



PLA bio-nanocomposites reinforced with cellulose nanofibrils (CNFs) for 3D printing applications

V. C. Agbakoba · T. C. Mokhena · E. E. Ferg ·
S. P. Hlangothi · M. J. John

Received: 7 September 2022 / Accepted: 6 October 2023 / Published online: 15 November 2023
© The Author(s) 2023

Abstract This study deals with the development of 3D printable bionanocomposites using poly(lactic acid) (PLA) with $\leq 2\%$ D-lactic acid content and cellulose nanofibrils (CNFs). The CNFs were extracted from the waste sawdust of *Eucalyptus grandis* via chemical and mechanical techniques. Thermogravimetric analysis (TGA) revealed that the CNFs were thermally stable within the intended processing temperature ranges. In this study, a combination of

solvent casting and melt extrusion techniques was adopted in the production of PLA containing 1 wt% and 3 wt% CNFs. The neat PLA filament was brittle and frequently broke during fused deposition modelling (FDM) 3D printing. However, the incorporation of triacetin as a green plasticizer resulted in improved filament flexibility and eliminated the inherent brittleness. TGA analysis revealed a slight reduction in the degradation temperature of the bionanocomposites when compared to neat polymer; however, all the specimens were thermally stable within the processing temperature. The scanning electron microscopy images of the 3D printed specimens revealed the presence of voids across the fracture surfaces. The tensile analysis of 3D printed specimens revealed that the PLA/CNF bionanocomposites exhibited higher tensile modulus, and elongation (strain) when compared to PLA-based specimens. The tensile strength of the 3D-printed 1 wt% bionanocomposite specimen was 12% higher than that of the neat specimen, whereas the 3 wt% bionanocomposite remained comparable to neat PLA. In summary, the morphological, tensile and 3D printing analysis revealed that the bionanocomposite filaments possessed adequate roundness, flexibility, and strength. The as-prepared filaments performed well under low printing temperatures without warping.

Supplementary Information The online version contains supplementary material available at <https://doi.org/10.1007/s10570-023-05549-2>.

V. C. Agbakoba · E. E. Ferg · S. P. Hlangothi · M. J. John
Department of Chemistry, Faculty of Science, Nelson
Mandela University, Port Elizabeth, South Africa
e-mail: s215161440@mandela.ac.za

V. C. Agbakoba · M. J. John
Centre for Nanostructures and Advanced Materials,
Chemicals Cluster, CSIR, Pretoria, South Africa

V. C. Agbakoba
Africa Earth Observatory Network-Earth Stewardship
Science Research Institute (AEON-ESSRI), Nelson
Mandela University, Gqeberha, South Africa

V. C. Agbakoba
Centre for Broadband Communication (CBC), Nelson
Mandela University, Gqeberha, South Africa

T. C. Mokhena (✉)
DSI/Mintek- Nanotechnology Innovation Centre,
Advanced Materials, Mintek, Randburg, South Africa
e-mail: mokhenateboho@gmail.com

Keywords Poly(lactic acid) · Cellulose nanofibrils · Bionanocomposites · Additive manufacturing · Fused deposition modelling printing

Introduction

There is a growing desire to adopt sustainable, eco-friendly, and renewable feedstock materials in 3D printing processes (additive manufacturing), injection moulding, extrusion, and thermoforming (Mokhena et al. 2018; 2021). Amongst these processing techniques, additive manufacturing merits special interest due to its attractive benefits. It is a simple production process that enables the manufacturing of products faster and at a relatively low cost while maintaining high precision. 3D printing is commonly employed to manufacture customized products tailored for specific applications with minimal waste. The FDM method is one of the most commonly used material extrusion 3D printing processes (Gohar et al. 2021; Mokhena et al. 2018). This printing technique involves the melt extrusion and layer-by-layer deposition of a molten thermoplastic filament according to a predetermined three-dimensional design (Özdilli 2021; Zou et al. 2016). The majority of FDM 3D printers today primarily use thermoplastic-based filaments as feedstock materials. These filaments are characterized by diameters ranging from 1.75 to 3.0 mm, depending on the specifications of the FDM 3D printer (Pan et al. 2016; Mohammed et al. 2017). The key benefits of FDM 3D printing include cost efficiency due to short lead times, the ability to fabricate complex parts, minimal waste generation, and energy efficiency.

Poly (lactic acid), an aliphatic polyester, is currently the most widely used thermoplastic biopolymer in FDM 3D printing (Mokhena et al. 2018; 2019; Mochane et al. 2019). The attraction towards PLA stems from its increasing availability, the potential for biodegradability, promising mechanical properties, and superior processability (Ferreira et al. 2017; Clarkson et al. 2020). Generally, high molecular weight PLA can either be semi-crystalline or amorphous, depending on the ratio and distribution of its L- and D- enantiomeric units (Modi et al. 2013; Mokhena et al. 2019). Nevertheless, the L-lactic acid is the most commonly occurring PLA stereoisomer. The overall ratio of stereoisomers and enantiomeric purity determines PLA's processability, crystallization behaviour, and mechanical and thermal properties (Modi et al. 2013; Mokhena et al. 2019). For instance, PLA containing 2 to 8% D- content is semicrystalline, meanwhile PLA with $\geq 10\%$ D- content is entirely amorphous (Jiang et al. 2010). However,

the applicability of unmodified PLA is mainly limited due to issues such as slow crystallization, poor melt strength, low heat distortion temperature, and inherent brittleness (Jonoobi et al. 2010; John et al. 2021). Nevertheless, the addition of natural-based reinforcing materials, such as cellulose nanofibrils (CNFs), is also known to further improve the crystallization behaviour and mechanical properties of PLA (John et al. 2021; Wang et al. 2017; Wang et al. 2020b). CNFs consist of dense networks of cellulose fibrils with amorphous and crystalline domains (Xie et al. 2020; Wang et al. 2020a). The high aspect ratio and remarkable axial strength of CNFs make them an ideal natural-based reinforcing agent (Wegst and Ashby 2004; Moon et al. 2011). Hence, bionanocomposites derived from renewable thermoplastic biopolymers and reinforcing fibres extracted from waste biomass residues present a viable FDM 3D printing feedstock. Several researchers have successfully employed bionanocomposite filaments in FDM 3D printing to produce prototypes and functional parts (John et al. 2021; Wang et al. 2017; Murphy and Collins 2018).

The reinforcing effect of CNFs is significantly hindered by weak interfacial interactions and inadequate dispersion within the PLA matrix. The fundamental hydrophilic nature of CNFs' surface chemistry, in contrast to the hydrophobic characteristics of PLA, is frequently identified as the primary factor leading to weak interfacial interactions. (Jonoobi et al. 2010; Armentano et al. 2013). Additionally, the strong attractive forces between the fibrillar networks of CNFs cause them to easily aggregate, making it difficult to attain effective dispersion within the PLA matrix. Several researchers have adopted the solvent-casting method as a viable means of mitigating early CNF agglomeration. (Wang et al. 2017; Chakraborty et al. 2006). In this procedure, CNFs are directly mixed into pre-dissolved PLA solution, cast into sheets, and subsequently dried. This approach effectively preserves the dispersed state of CNFs within the matrix. Nevertheless, it's important to acknowledge that solvent casting does have limitations. Concerns revolving around toxicity and the substantial volume of solvent required to render this technique unsuitable for industrial-scale applications. The commonly used solvents for the dissolution of PLA include chloroform, dichloromethane,

tetrahydrofuran, and 1,3-dioxane (Sato et al. 2013; Jonoobi et al. 2010).

Several reports have demonstrated the application of solvent casting for creating concentrated PLA/CNF masterbatches, which are then used for producing bionanocomposites through conventional melt processing methods (Jonoobi et al. 2010; Bei Wang and Sain 2007; Murphy and Collins 2018). For instance, Iwatake et al. (2008) investigated the sustainable production of microfibrillated cellulose-reinforced-PLA bionanocomposites. They compared the effects of solvent casting and direct mixing methods, revealing that superior dispersion of microfibrillated cellulose in PLA can be achieved through pre-mixing in organic solvents followed by kneading using a rotary mixer. Furthermore, the compatibility and flexibility of PLA/CNF bionanocomposites can be improved using green plasticizers (e.g., triacetin (TA), triethyl citrate (TEC), tributyl citrate (TBC), acetyl-tributyl citrate (TBAC)) (Ljungberg and Wesslen 2002; Paul et al. 2021; Clarkson et al. 2020; Harte et al. 2013). The study conducted by Herrera et al. (2015) reported significant improvement in ductility, compatibility, and toughness of PLA/CNF bionanocomposites upon the addition of TA. Furthermore, the investigation conducted by Ljungberg and Wesslen (2002) revealed that the miscibility of PLA and TA can be attributed to their closely matched solubility parameters.

Currently, semicrystalline PLA grades with 4% D-lactic acid content are the most used feedstock in the production of 3D printable bionanocomposite filaments (Dong et al. 2017; Wenyang Xu et al. 2018; Li et al. 2019; Tekinalp et al. 2019). This is due to their desirable processibility, and mechanical properties. However, the growing demand for PLA-based filaments in FDM 3D printing applications necessitates a broader range of PLA grades to be considered as feasible feedstock options. While PLA grades with $\leq 2\%$ D-lactic acid content are more readily crystallizable, they are however very brittle and difficult to process into 3D printable filaments. Furthermore, there is a limited body of literature addressing the concerns related to the application of $\leq 2\%$ D-lactic acid content PLA grades in the production of 3D printable filaments.

The primary objective of this study is to develop a bionanocomposite using a PLA grade containing 2% D-lactic acid, cellulose nanofibrils (CNFs), and a biobased plasticizer. The approach taken in this study

focuses on utilizing environmentally friendly feedstock materials, employing low extrusion temperatures, and minimizing processing cycles. Prior research by Wang et al. (2020b) indicated that incorporating 2.5 wt% CNFs led to a noticeable enhancement in the mechanical properties of PLA. However, when CNF loadings surpassed 3 wt%, substantial fibrillar agglomerations formed within the PLA matrix (Wang et al. 2020b). In our present work, we have chosen to utilize CNF loadings of 1 and 3 wt% to achieve maximum benefits while minimizing the risk of significant agglomeration that could potentially cause blockages in 3D printer nozzles. The CNFs were extracted from forestry waste residues, specifically sawdust, through chemo-mechanical methods. PLA/CNF masterbatches were prepared using a combination of solution casting and melt extrusion. Subsequently, a single-screw extruder was employed to convert pelletized PLA/CNF bionanocomposites into a filament form. To enhance the processibility, flexibility, and compatibility of the PLA/CNF bionanocomposites, an optimized quantity of triacetin (TA) was introduced as a green plasticizer. The method outlined above yielded FDM 3D printable bionanocomposite filaments that exhibited an adequate balance between strength and flexibility. The chemical, thermal, mechanical, and morphological properties of the PLA/CNF bionanocomposites were thoroughly assessed and discussed.

Materials and methods

Materials

Poly(lactic acid) (PLA), Ingeo™ PLA6202D (semicrystalline; Mw = 140 kDa and $< 2\%$ D-lactide) with melting point 155–170 °C was procured from NatureWorks, Minnetonka, MN, USA). Triacetin (glycerol triacetate) with a density of $\sim 1.16 \text{ g cm}^{-3}$ at 20 °C was procured from Merck. Through a preliminary analysis, it was determined that 10 wt% was the optimal quantity of triacetin (TA) plasticizer, as elaborated in the supplementary information provided in S1 and S2. The cellulose nanofibrils (CNFs) were extracted from *Eucalyptus grandis* sawdust, which was sourced from the CSIR Biorefinery Industry Development Facility (BIDF) situated in Durban, South Africa.

Experimental methods

Extraction of cellulose nanofibrils (CNFs) from sawdust

Sawdust was treated with 1 wt% sodium hydroxide (NaOH) at 80 °C for 4 h under constant mechanical stirring to remove hemicellulose components. This process was repeated four times. Following each treatment, the remaining solid components were separated and washed with deionized water until achieving a neutral pH. Further bleaching treatment was performed twice at 80 °C for 6 h using a solution of 5% active sodium hypochlorite (NaClO) to remove the lignin components, leaving behind cellulosic fibres. After each bleaching treatment, the solid constituents (cellulosic fibres) were separated and rinsed with deionized water until a neutral pH. Subsequently, a fibrillation step was conducted using a friction grinder (MKCA6-39 Supermass collider, Masuko Sangyo Co, Ltd., Japan) operated at 1500 rpm. The cellulosic fibres were passed through the friction grinder multiple times for 20 min to achieve fibrillation. The resulting cellulose nanofibrils (CNFs) were then subjected to solvent exchange into acetone using centrifugation at 10 °C and 10,000 rpm for 10 min.

Preparation of PLA/CNF bionanocomposites

PLA/CNF masterbatch A preliminary mixture of solvent-exchanged CNFs and PLA was created using the solvent-casting technique. Approximately 50 g of PLA was fully dissolved in a beaker containing a mixture of acetone and chloroform in a ratio of 9:1. This beaker was then positioned within a water bath set at a temperature of 50 °C. Gradually, the solvent-exchanged CNFs were introduced into the dissolved PLA and thoroughly mixed utilizing an overhead stirrer. Subsequently, the PLA/CNF mixture was poured into aluminium baking trays and placed in a vacuum

chamber to facilitate solvent evaporation. The PLA/CNF masterbatch was further dried for 8 h at 50 °C, then cut into small pieces and securely stored within an airtight bag for subsequent processing.

Melt-mixing of PLA/CNF bionanocomposites

Melt-mixing was executed within a twin-screw co-rotating extruder (CTE-20, Coperion, China), equipped with seven distinct heat-controlled zones and boasting a compression ratio of 40 L/D. The PLA/CNF masterbatch was combined with unprocessed PLA to achieve CNF loadings of both 1% and 3%. The final extrusion temperature profile listed in Table 1 was adopted during the melt-processing of PLA and the bionanocomposites. Throughout the process, the twin-screw speed was consistently maintained at 50 rpm for all samples. The samples were pelletized and stored in airtight packaging for further processing.

Filament production on a single-screw extruder

The PLA and PLA/CNF pellets were manually pre-blended with 10% triacetin (TA) before filament extrusion. The TA plasticizer was readily absorbed by the PLA causing the pellets to adhere to each other as shown in Fig. 1. Filament production was performed on a pilot-scale single-screw extruder featuring five heat-controlled zones (see Fig. 1). The temperature profile applied across these five heating zones during filament extrusion was configured as follows: 70, 150, 160, 150, and 150 °C. As the hot filament exited the 2 mm nozzle, it was carefully guided into a cold-water bath. A motorized co-rotating pulling system with adjustable speed was used to draw the filament to ensure a consistent diameter. The diameter of the filament was determined by taking an average of multiple diameter readings along a 1-m filament sample length. Diameter measurements were performed using a Vernier caliper and the average values are

Table 1 Melt-extrusion temperature profile of the twin-screw extruder

Mixing profile	Temperature profiles (°C)							Screw speed. (rpm)
	Zone 1	Zone 2	Zone 3	Zone 4	Zone 5	Zone 6	Zone 7	
PLA	150	155	160	165	160	160	165	50
PLA/CNF	145	150	150	155	155	150	150	50

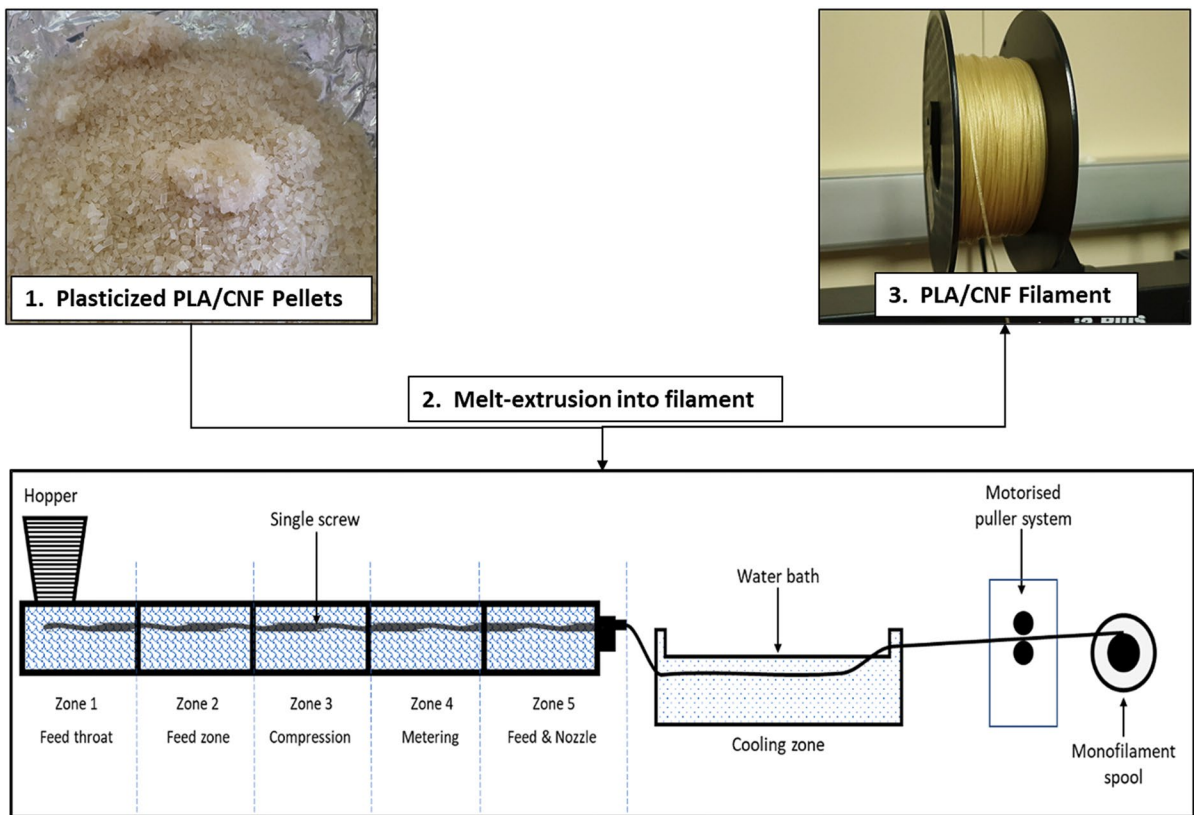


Fig. 1 An illustration showing the PLA-CNF monofilament production setup

Table 2 Formulation of FDM 3D printable filaments

Sample Description ^a	Final composition (%)			Filament diameter (mm)
	PLA	CNFs	Triacetin	
6Neat ^b	100	0	0	1.74 (± 0.06)
6BlankTA10 ^c	90	0	10	1.53 (± 0.08)
TA10CNF1% ^d	89	1	10	1.65 (± 0.09)
TA10CNF3% ^e	87	3	10	1.66 (± 0.03)

^aSamples were dried at 50 °C before extrusion

^bSample contains only neat PLA6202D

^cSample contains PLA6202D and triacetin

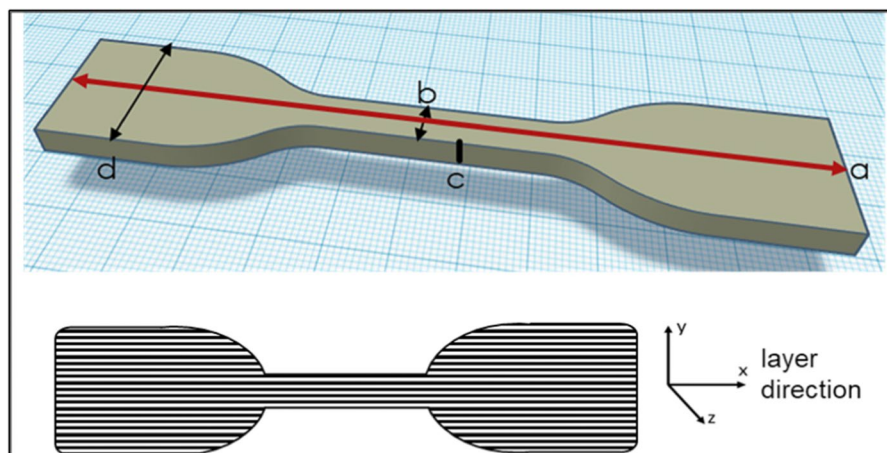
^{d,e}Sample contains PLA6202D, cellulose nanofibrils (CNFs) and triacetin

listed in Table 2. Finally, the filaments were dried in an oven for 5 h at 50 °C before 3D printing.

Design and 3D printing of tensile test specimen

The stereolithography (STL) computer-aided design (CAD) of the dumbbell shape was designed to adhere to the specifications outlined in Fig. 2. The dumbbell-shaped tensile specimens were 3D-printed using a fused deposition modelling (FDM) desktop 3D printer (WANHAO Duplicator i3). The dumbbell-shaped specimens were printed flat on the build plate (x, y-axis). Consistently, all specimens were printed at a temperature of 175 °C, with a print speed of 60 mm/sec. The layer height was set to 0.2 mm, this represents the specified height of individual PLA extrudate laid out by the printer nozzle. Each specimen was printed with 2 external perimeter walls and 5 bottom/top layers. Since only solid dumbbells were needed for this experiment, the infill settings were set to 100%. The infill pattern followed a concentric direction, with a 90° infill line direction. Following the printing process, the dimensions of the resulting 3D-printed

Fig. 2 3D rendition of the dumbbell-shaped test specimen (top) showing the layer direction (bottom). Where: $a = 115$ mm, $b = 6$ mm, $c = 4$ mm, $d = 20$ mm



dumbbell specimens were accurately gauged using a ULTRA CAL VI Vernier calliper (Fowler High Precision, Massachusetts, USA).

Characterization techniques

Chemical analysis

The chemical composition analysis was performed using an Attenuated Total Reflectance—Fourier transform infrared spectrometer (ATR-FTIR) (BRUKER TENSOR II, MA, USA). The FTIR spectra of the samples were recorded between $4000 - 600$ cm^{-1} , using 32 scans, at a 4 cm^{-1} resolution. The background spectrum was recorded before analysing each sample. The cellulose nanofibrils were dried in a convection oven set at 80 $^{\circ}\text{C}$ for 12 h before testing. Conversely, the PLA and PLA/CNF bionanocomposites were conditioned at a temperature of 50 $^{\circ}\text{C}$ for 6 h before FTIR analysis.

X-ray Powder Diffraction (XRD)

The X-ray diffraction (XRD) patterns of the *eucalyptus* sawdust (SD), and cellulose nanofibrils (CNFs) were measured using a benchtop powder X-ray diffractometer (BRUKER D2 PHASER, MA, USA). The diffraction pattern of oven-dried CNFs was recorded and compared to the plain sawdust. The CNF gel was dried in a convection oven set at 80 $^{\circ}\text{C}$ for 2 h and conditioned at 50 $^{\circ}\text{C}$ for 3 h before testing. The X-ray diffraction (XRD) patterns of the CNF samples were measured over the $2\theta = 5^{\circ} - 50^{\circ}$ angular range with a

scanning step of $0.02^{\circ}/\text{step}$ and 4 secs per step with sample rotations using a $\text{Cu K}\alpha 1$ and $\text{K}\alpha 2$ radiation source with $\lambda = 0.15406$ nm / 0.15445 nm (weighted average 0.15418 nm). A Ni filter was used at the Primary Beam to reduce the effect of the $\text{K}\beta$ radiation. A Silicon (Si) zero background sample holder was used, and the sample rotated in the horizontal plane at 10 rotations/min. In addition, a 3 mm air scatter slit was in place to reduce the low-angle erroneous air scattering that could be misinterpreted.

The degree of crystallinity (I_c) was determined via the deconvolution method using Topas v6 software (Germany) that allows for full pattern Rietveld refinement of the diffraction pattern. The crystallographic information framework (.cif) file for the crystal structure of the crystalline phase of cellulose-I β was obtained from the open-source Crystallography Open Database (COD) (Vaitkus et al. 2021). The .cif file used was from the structural study of cellulose-I β conducted by Nishiyama et al. (2002). The refinement procedure and parameter settings inputted in Topas software will be highlighted in the results and discussion section.

Morphological analysis

The morphology of the cellulose fibres (CFs) after the removal of hemicellulose and lignin was observed using scanning electron microscopy (SEM) (JEOL JSM-IT100, Peabody, USA). About 0.1 mg of the CFs was diluted with 50 mL of ethanol and sonicated to avoid aggregation. A small amount of the CFs was deposited on a copper grid and dried at 120 $^{\circ}\text{C}$ for

6 h. Upon drying, the specimen was gold-coated and was conditioned at 35 °C for 30 min before analysis.

The cellulose nanofibrils (CNFs) obtained after successive defibrillation steps using the friction grinder were observed by transmission electron microscopy (TEM) using a JOEL 2100 TEM operated at 200 kV accelerating voltage. The CNFs were deposited onto a carbon-coated grid by dipping the grid into a dilute suspension of CNFs and then drying the grid in a vacuum oven overnight. The diameters of the CNFs were determined using an image analysis program (ImageJ 1.37v), and an average of 100 measurements was used.

The transverse and cross-sectional area of the filament samples were examined under a Leica S6D Greenough stereo microscope with 6.3:1 zoom (Leica Microsystems, Germany). Images were captured using a 3.1 Megapixel Leica EC3 colour camera (Leica Microsystems, Germany) at 20× magnification. The bottom part of the specimen was lit using cross-polarized light, whilst normal light was shone on the surface specimen. The high-contrast images acquired from this analysis were possible due to the combination of different light sources.

The fractured surfaces of the 3D-printed dumbbell tensile specimens were also observed using scanning electron microscopy (SEM) (JEOL JSM-IT100, Peabody, USA). The specimens were gold-coated and conditioned at 35 °C for 30 min before analysis.

Thermal analysis

Thermal analysis of CNFs, PLA, and PLA/CNF bionanocomposite filaments was performed on a thermogravimetric analyzer (TGA5500, TA instruments New Castle, USA). Samples with masses of about 8.6 mg were heated under a nitrogen flow of 100 mL min⁻¹ from ambient temperature (~30 °C) to 600 °C at a heating rate of 10 °C min⁻¹. Platinum samples and reference pans were used for this experiment.

Determination of density

The densities of the 3D printed tensile specimen were measured according to Archimedes' principle using ethanol (≥99.8% (GC) as an auxiliary liquid at ambient temperature (26 °C). The mass of six samples of each specimen was recorded in air and when completely immersed in ethanol using an

analytical balance accurate to 0.0001 g. The relative density of each specimen was calculated according to Eq. (1), where m_a is the mass of the sample in air, m_{et} is the mass of the sample in ethanol, and ρ_{et} is the density of ethanol (0.7841 g/cm³ at 26 °C). The density of 6202D PLA pellets was determined as 1.2067 ± 0.08 g/cm³ using the same method. All the specimens were vacuum-dried at 50 °C for 8 h before the commencement of analysis.

$$\text{Density}(\rho) = \frac{m_a}{m_a - m_{et}} \times \rho_{et} \quad (1)$$

Uniaxial tensile analysis

Uniaxial tensile analysis of the bionanocomposite filaments and 3D-printed dumbbell-shaped tensile specimens was performed according to ASTM D638. The tensile data was recorded using a Tinius Olsen 10ST Benchtop tensile tester, fitted with a 10kN load-cell. The filaments were pulled using a rubber-padded HT400 pneumatic grip (Horsham, USA) to minimize the clamping stress exerted on the filaments, whereas a mechanical wedge grip was used for the dumbbell specimen. The analysis was performed at a gauge length of 25 mm, whilst applying 2 MPa pre-load to prevent sample slippage. All the samples were conditioned in a convection oven set at 50 °C for 12 h before testing. The tensile results reported were an average of five measurements.

Results and discussion

Morphological analysis of cellulose nanofibrils (CNFs)

The surface morphology of cellulose fibres (CFs) after chemical treatments was studied using Scanning Electron Microscopy (SEM). The SEM micrograph in Fig. 3A shows a dense network of cellulose fibres after the successful removal of hemicellulose, pectin, and lignin. The width of these cellulose fibres was found to vary within the range of 7.4 µm to 8.2 µm. Subsequently, Transmission Electron Microscopy (TEM) was employed to visualize the cellulose nanofibrils (CNFs) that were obtained through successive milling of the cellulose fibres using an

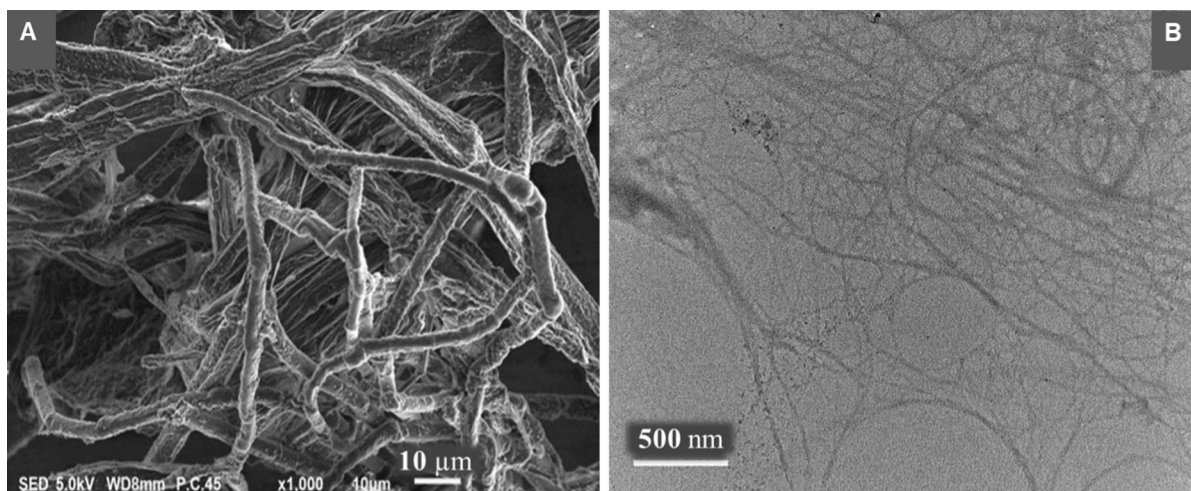


Fig. 3 SEM image of cellulose fibre obtained after delignification and removal of hemicellulose (left), and TEM image of the cellulose nanofibrils (CNFs) obtained after ultra-fine friction grinding of cellulose fibres (right)

ultra-fine friction grinder. In Fig. 3B, the TEM micrograph illustrates an intricate network of interconnected de-fibrillated CNFs, exhibiting diameters ranging from 2 to 30 nm. It's noteworthy that while plant-based cellulose originally existed in large clusters (Fig. 3A), the combination of chemical treatment and ultra-fine friction grinding techniques applied in this study led to their defibrillation into individual fibrils, as shown in Fig. 3B.

Crystallinity analysis of CNFs

Figure 4 and 5 shows the X-ray powder diffraction patterns of the sawdust (SD) of *Eucalyptus grandis* softwood and the cellulose nanofibrils (CNFs). The X-ray diffraction patterns were subjected to a Rietveld refinement analysis using Topas v6 software. The approach used in determining the degree of crystallinity of the samples was adapted from the review work published by Terinte et al. (2011). The general idea is that the diffraction pattern is made up of the contribution of the crystalline and the amorphous phases

Fig. 4 PXRD pattern of cellulose nanofibrils (CNFs) refined with the cellulose-I β structural diffraction pattern and a single amorphous halo. Diffraction data (black line), Fitted data (red line), Refined cellulose-I β (blue line), Amorphous halo (green line) with the peak maximum at $2\theta = 22.1$ (vertical black line), Difference plot (grey line), Background fit (sloping straight grey line), Blue line on the x-axis indicates the peak positions

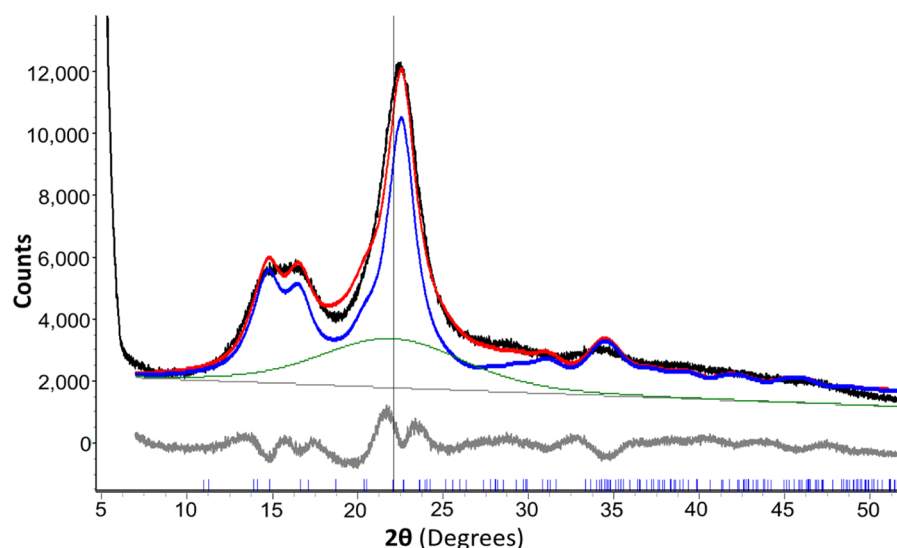
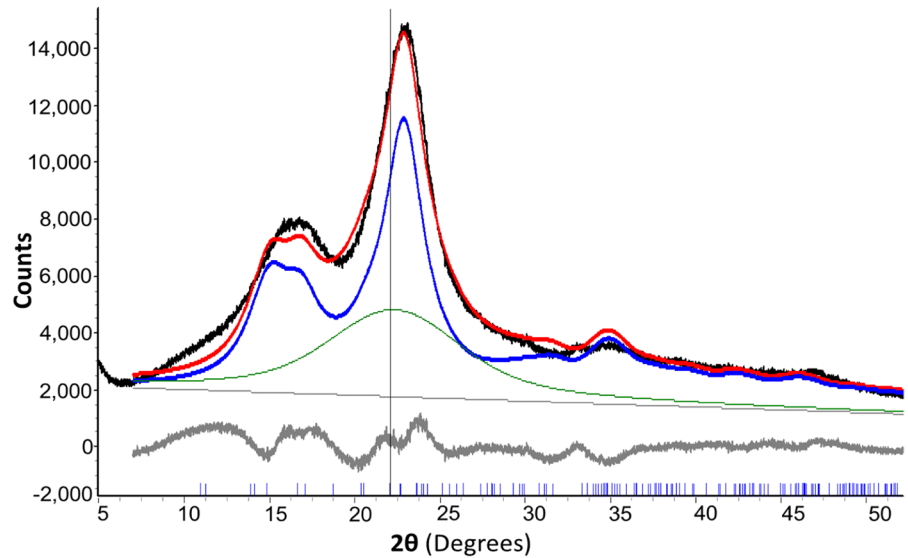


Fig. 5 PXRD pattern of *Eucalyptus grandis* sawdust (SD) refined with the cellulose- $I\beta$ structural diffraction pattern and a single amorphous halo. Diffraction data (black line), Fitted data (red line), Refined cellulose- $I\beta$ (blue line), Amorphous halo (green line) with the peak maximum at $2\theta = 22.1$ (vertical black line), Difference plot (grey line), Background fit (sloping straight grey line), Blue line on the x-axis indicates the peak positions



of the material. The prominent amorphous halo can be simplistically modelled with a single broad diffraction peak whereas the contribution of the crystalline phase would come from the sharper diffraction peaks. Full pattern Rietveld refinement allows for the use of a fundamental parameters approach to match the diffraction pattern to a known crystal structure contained typically within a crystallographic information framework (.cif) or structure file format (.str) file. This not only allows for the scaling and matching of theoretically determined structural parameters and various instrumental parameters to the determined diffraction pattern but also allows for the determination of other material properties such as crystallite size and preferred orientations.

The crystal structure parameters of the cellulose phase with space group P21 obtained from the.cif file of Nishiyama et al. (2002) and the unit cell dimensions ($a = 0.7892$ nm, $b = 0.8112$ nm, and $c = 1.036$ nm) reported by Muller et al. (2006) were fixed during the refinement. A Pearson VII-shaped peak was used during the refining step to allow for some slight asymmetric fitting of the amorphous peak contribution. The background was set to a Chebychev first-order polynomial and initially allowed to be refined to give a reasonable straight-line background fit. This was subsequently fixed to prevent

unnecessary shifting of the background during subsequent refinement steps. The amorphous halo was fitted to a constant crystallite size of 1.2 nm and the Gaussian crystallite size broadening parameter was fixed at 1.3 for both patterns. The sample displacement correction was allowed during the refinement. The amorphous contribution is shown by the broad signal with a single peak near $2\theta = 22.1^\circ$ in Figs. 4 and 5. The shape of the amorphous contribution of the CNF roughly resembles what has been reported in the literature (Agarwal et al. 2021). The Lawrencian crystallite size parameter L in the structural file of cellulose $I\beta$ was refined to determine the volume-weighted mean crystallite size (LVol-IB) based on the full-width half maximum (FWHM) and the integral breadth using the full peak profile. The Chebychev background was allowed to be re-refined as a final step to allow for a better-weighted profile R-factor (R_{wp}) fit and was subsequently fixed again. The value of the weighted profile R-factor (R_{wp}) deduced after the Rietveld refinement was $R_{wp} = 7.1$ (CNFs) and $R_w = 6.7$ (SD), confirming reasonable model fitting. The volume-weighted mean crystallite size (LVol-IB) was determined as 3.0 nm for the CNF and 2.1 nm for the SD sample respectively. The slight increase in LVol-IB could be due to the removal of non-cellulosic components

and increased exposure of cellulose crystalline domains present in the CNFs. The degree of crystallinity was determined by dividing the contribution of all the crystalline peak areas over the total peak area (Area of crystalline phase/ (Area of crystalline phase + Area of amorphous phase)). The degree of crystallinity (I_c) was determined as 79.3% for CNFs and 73.1% for SD respectively. The difference in the I_c which is indicative of the presence of highly ordered crystalline structure is partly attributed to the sharper (200) peak of CNFs.

Thermogravimetric analysis of cellulose nanofibrils

The thermogravimetric weight loss (TG) and the derivative weight loss (DTG) profile of cellulose nanofibrils (CNFs) are shown in Fig. 6. The initial weight loss of approximately 8.7% occurring within the temperature range of 60 to 150 °C is attributed to the elimination of moisture and volatile components (Mtibe et al. 2015). An onset of degradation was observed at 220 °C and is attributed to the decomposition of low molecular weight constituents within the CNFs. The main degradation peak of CNFs emerges at 325 °C, coinciding with the processes of dehydration, depolymerization, and the decomposition of glycosidic bonds (Yousefi et al. 2013). Furthermore, about 24.7% of residual ash content remained at 600 °C. Based on the TGA results, it is evident that the

CNFs remain stable within the processing temperature range of the chosen PLA material.

Chemical analysis of CNF, PLA, and PLA/CNF bionanocomposites

In Fig. 7, the FTIR spectra of TA, sawdust, CNFs, neat PLA, and bionanocomposites are presented. Notably, the broad transmittance peak at 3390 cm^{-1} in the CNFs spectra corresponds to the stretching vibrations of hydroxyl groups (O–H) (Wang et al. 2020b). The absence of peaks at 1500 , 1590 and 1740 cm^{-1} for CNFs indicates the removal of hemicellulose and lignin (Kouadri and Satha 2018). The removal of these groups upon chemical and mechanical treatments has been reported elsewhere (Kouadri and Satha 2018; Motaung and Mtibe 2015). The fingerprint region of the CNFs spectra reveals transmittance peaks at 1160 cm^{-1} , 1050 cm^{-1} , and 895 cm^{-1} , corresponding to stretching vibrations of C–O–C, C–OH glucose, pyranose ring, and β -glycosidic bending vibrations (Rasheed et al. 2020; Tonoli et al. 2016). Similarly, the FTIR spectrum of the neat PLA filament (6Neat) displays all characteristic absorption bands typical of PLA (Kister et al. 1998). The transmittance peak from stretching vibrations of CH_3 groups is assigned to the peaks around $3000\text{--}2900\text{ cm}^{-1}$.

Fig. 6 Thermal decomposition of cellulose nanofibrils (CNF) (red dashed lines represent DTG curve)

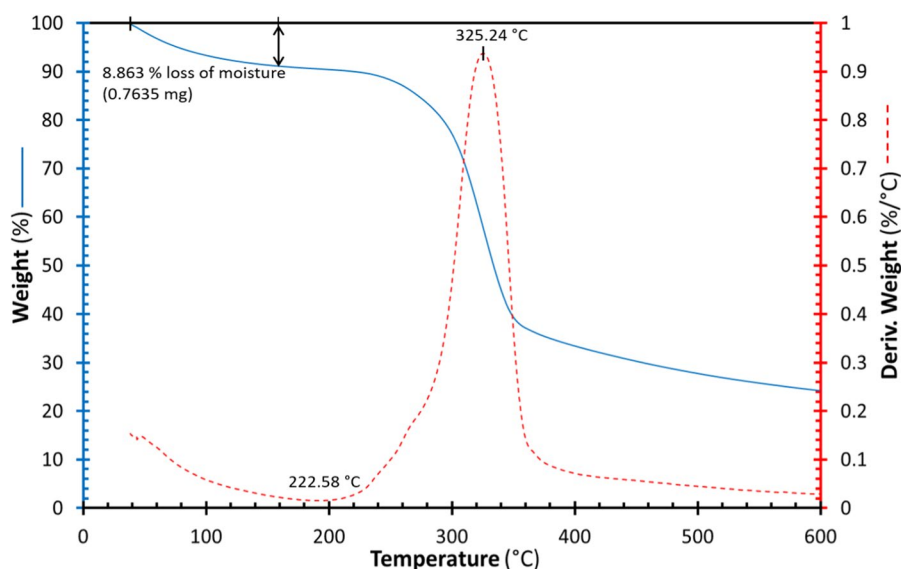
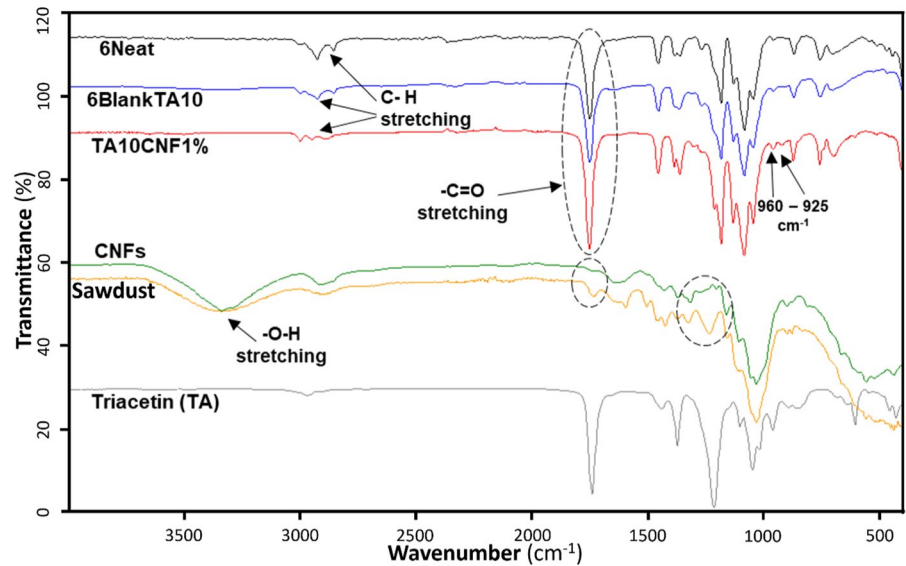


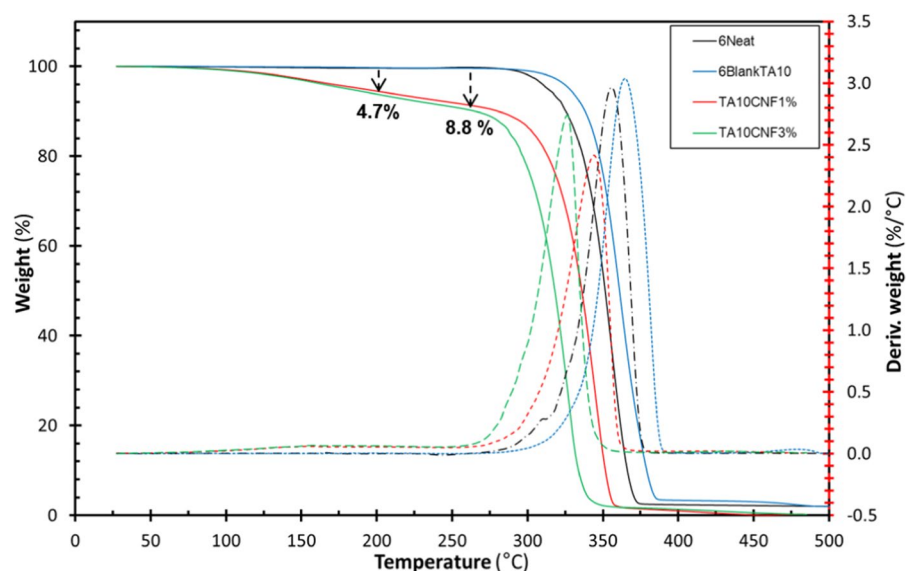
Fig. 7 ATR-FTIR profiles showing the chemical composition of TA (black), sawdust (orange), CNFs (green) 6Neat (black), 6BlankTA10 (blue) and TA10CNF1% (red)



The intensity of the carbonyl ($C=O$) stretching vibrations of PLA assigned to the 1750 cm^{-1} peak shows a noticeable increase in the presence of triacetin. This increase in intensity is attributed to the combined stretching vibrations of $C=O$ groups present in both PLA and triacetin. The asymmetric bending vibrations of CH_3 are assigned to the 1450 cm^{-1} peak, 1260 cm^{-1} is assigned to carbonyl ($C=O$) bending vibrations, whilst the skeletal stretching vibrations

of the PLA-ester ($C-O-C$) groups are assigned to $1200\text{--}700\text{ cm}^{-1}$ peaks. Furthermore, in the spectra of TA10CNF1%, the peaks at 960 cm^{-1} and 925 cm^{-1} are attributed to amorphous and crystalline vibrations of PLA (Beltrán et al. 2016). However, the amorphous peak at 925 cm^{-1} is hardly noticeable in 6Neat and 6BlankTA10 samples. This suggests an increase in crystallinity in both samples compared to TA10CNF1%. Finally, the FTIR spectra of triacetin show a signal at 1755 cm^{-1} assigned to the $C-O$ stretch (Lacerda et al. 2015).

Fig. 8 Thermal decomposition profiles showing thermogravimetric (TG) and derivative thermogravimetric (DTG) curves of the filaments



Thermal Analysis of PLA and PLA/CNFs bionanocomposite filament

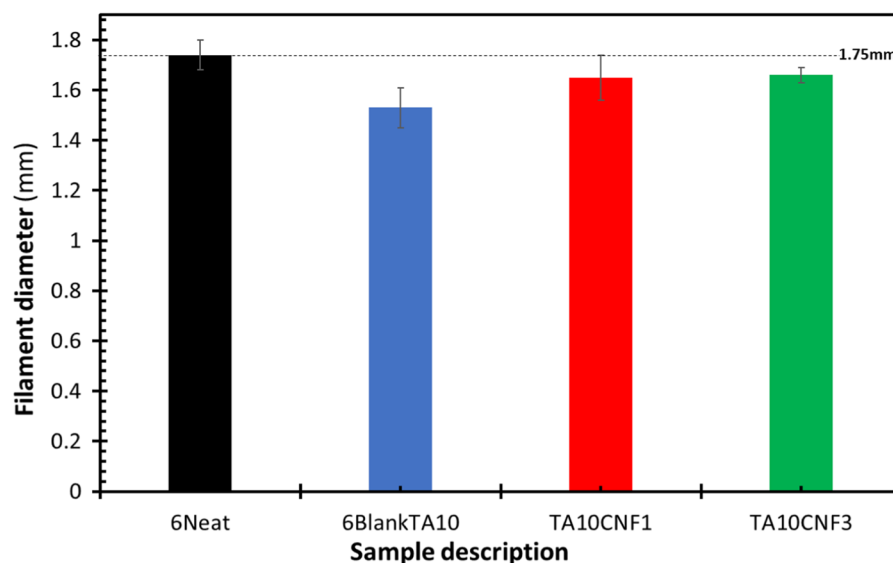
Figure 8 shows thermogravimetric (TG) and derivative thermogravimetric (DTG) plots of the filament samples. The thermal decomposition of PLA is generally attributed to hydrolysis, zipper-like depolymerization, oxidative random chain scission, and intramolecular transesterification (Södergård and Stolt 2002). Notably, the 6Neat filaments display a distinct single-step thermal degradation behaviour that initiates at 303 °C and reaches its peak at 354 °C (Table 3). The addition of triacetin (TA) (6BlankTA10), however, resulted in an increase in thermal stability with the onset degradation temperature at 310 °C and peaking at 366 °C (Table 3). This 7 °C increase in the onset of degradation is attributed to the increased crystallinity and minimal hydrolysis of PLA polymer chains. The crystalline domains in PLA require more thermal energy to decompose compared to amorphous domains. Contrastingly, the bionanocomposite filament (TA10CNF1%) showed a ~10 °C decrease in both onset and peak degradation

temperatures compared to neat PLA filament (6Neat). The TG profile of both bionanocomposite filaments exhibits a 2-step weight loss, as shown in Fig. 8. The initial weight loss is attributed to the evaporation of moisture and TA plasticizer. About 4.7 wt% of the volatile material was lost at 200 °C and 8.8 wt% at 250 °C. The evaporation of the plasticizer could have been exacerbated during PLA crystallization and phased separation of TA. Plasticizers, such as TA, have been reported to increase molecular mobility, consequently leading to faster crystallization during cooling (Martin and Avérous 2001). However, Ljungberg and Wesslen (2002) reported that an increase in PLA crystallization resulted in the expulsion of TA. This is attributed to the plasticizer (TA) being miscible solely within the amorphous domains of PLA. The moisture adsorbed on the surface of the CNFs could have induced hydrolytic degradation of the PLA molecular chains. This hydrolysis-driven thermal degradation was more pronounced in the TA10CNF3% bionanocomposite filament, which incorporated higher CNF loadings (evidenced by an onset temperature of around ~280 °C and a peak

Table 3 Comparison between the onset and peak degradation temperatures

Degradation temperature (°C)	Sample description			
	6Neat	6BlankTA10	TA10CNF1%	TA10CNF1%
Onset	303.36 (±0.17)	310.35 (±0.17)	292.66 (±0.17)	279.66 (±0.17)
Peak	354.01 (±0.15)	366.29 (±0.18)	345.59 (±0.17)	327.45 (±0.17)

Fig. 9 The variation in filament diameter (the dotted line represents the standard filament diameter)



temperature of around ~ 328 °C) (Table 3). However, the early-stage thermal degradation occurred above the temperature (175 °C) used during the 3D printing of the bionanocomposite filaments.

Comparison of PLA and PLA/CNF bionanocomposite filament diameter

The variation of the measured filament diameter compared to the expected diameter is represented in Fig. 9. Presently, filaments with a diameter of 1.75 mm are widely used in most FDM-based 3D printing activities. The Chinese National Standard (GB/T 37643–2019) specifies a diameter tolerance of ≤ 0.05 mm for these filaments. The diameter of the 6Neat filament of $1.74 (\pm 0.06)$ mm falls within the expected tolerance range. Conversely, the 6BlankTA10 sample had the smallest filament diameter of all the examined samples at $1.53 (\pm 0.08)$ mm. Nonetheless, a slight reduction in filament diameter is observed for filament samples containing cellulose nanofibrils (CNFs). The filament diameter for the samples containing 1% and 3% CNFs was $1.65 (\pm 0.09)$ mm and $1.66 (\pm 0.03)$ mm, respectively.

A succession of factors is postulated to account for the observed reduction in filament diameter in the presence of TA. Primarily, an increase in polymer chain mobility due to plasticization typically translates into reduced melt viscosity and melt strength. As a result, the reduction in melt strength and the low melt viscosity combine to cause the PLA filament to thin out as it emerges from the extruder nozzle. Secondly, the decrease in filament diameter could be attributed to thermal shrinkage. This likely occurred during the phase separation of the plasticizer from the PLA matrix. This is because the plasticizer (TA) is only miscible with the amorphous PLA domain. So, the TA was likely expelled during crystallization as previously reported by (Ljungberg and Wesslen 2002). Furthermore, the phase separation of TA and PLA was likely exacerbated by the cumulative interplay of processing conditions (temperature, compression, screw speed, and cooling rate). Lastly, the reduction in filament diameter could also be caused by the tension exerted during filament winding (spooling). This is because the filament remains

quite pliable after exiting the cooling zone during extrusion. Nevertheless, the addition of cellulose nanofibrils (CNFs) seemed to reduce filament thinning. This could be attributed to the increased melt viscosity and the consequent reduction in PLA polymer chain mobility, stemming from the incorporation of CNFs. Additionally, the presence of CNFs in the bionanocomposite filament might have absorbed the exuded TA, thus mitigating the loss of plasticizer during processing.

Morphological of filaments

Figure 10 shows the visual appearance of the surface and cross-sectional characteristics of all filament samples. The high surface roughness of the 6Neat filament is attributed to inadequate processability (melt, cooling, and flow behaviour) during filament extrusion. The addition of TA plasticizer resulted in improved processability, and reduced surface roughness of the 6BlankTA10 filament. However, the surface smoothness decreased after the incorporation of cellulose nanofibrils (CNFs), as seen in Fig. 10. Furthermore, the cross-sectional images show inconsistent filament roundness for 6Neat and 6BlankTA10 specimens (insert Fig. 10), which is likely caused by the poor melt and compressive strength of PLA during the extrusion process. However, the filaments containing 1% and 3% CNFs showed improved roundness, which can be attributed to improved compression and bulk density. Additionally, the high contrast between the CNFs anisotropically dispersed within the PLA matrix can be visualized in Fig. 10. The image contrast reveals that the entanglement of the otherwise dense fibrous networks of CNFs into micrometre-long domains occurred during filament production. The hydrophilicity of CNFs contributes to a higher likelihood of agglomeration during processing. Thus, explains the challenge of attaining uniform CNF dispersion within the polymer matrix.

Tensile behaviour of filaments

The tensile properties of the filaments are summarized in Table 4. The lowest tensile strength of 22.5 ± 3.8 MPa and % elongation at break of

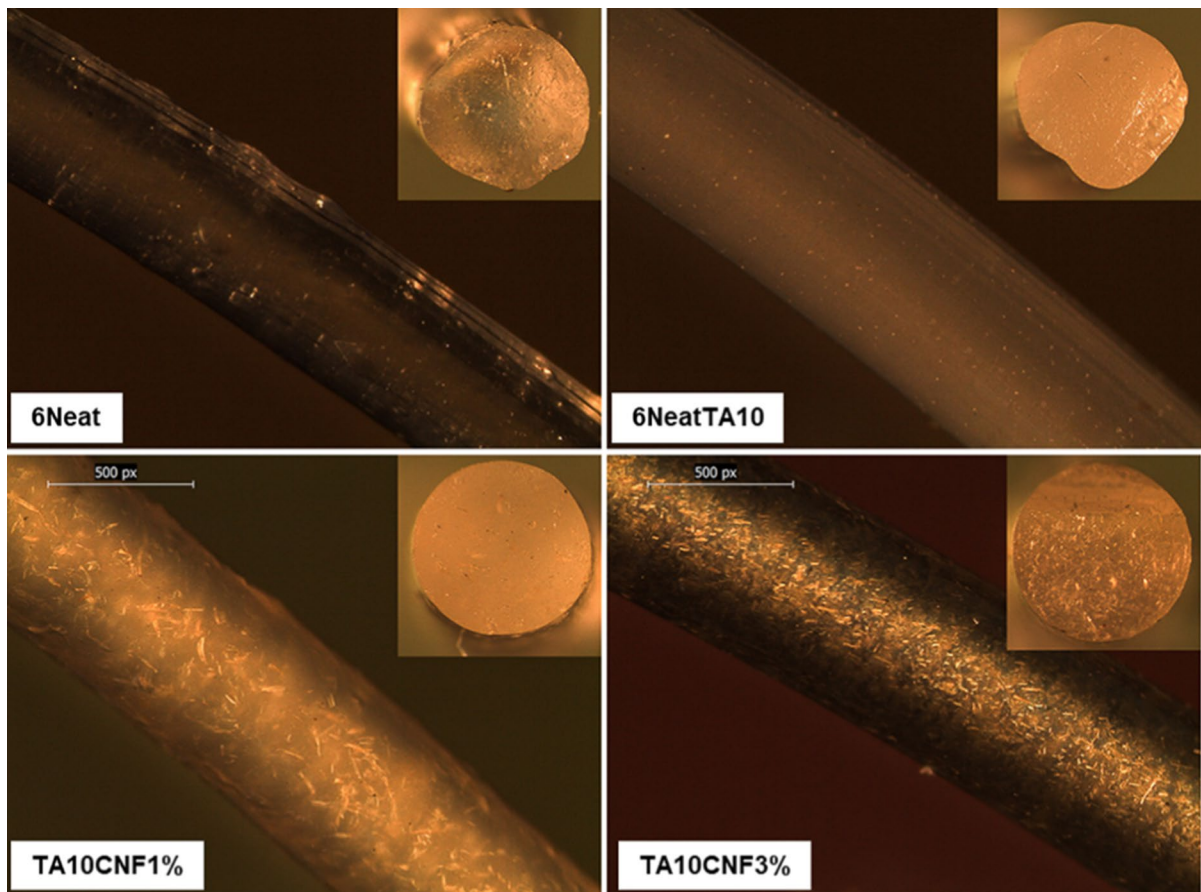


Fig. 10 The surface and cross-sectional (inserts) morphology of filament specimens imaged at $\times 40$ magnification using a compound microscope under cross-polarized light

Table 4 Results from the tensile analysis of developed filaments

Sample description	Tensile strength (MPa)	Elongation at Break (%)	Maximum breaking force (N)
6Neat	22.50 (± 3.80)	0.30 (± 0.05)	53.53 (± 9.00)
6BlankTA10	40.08 (± 1.80)	2.66 (± 0.70)	65.25 (± 3.30)
TA10CNF1%	29.26 (± 1.80)	6.13 (± 1.10)	53.74 (± 3.40)
TA10CNF3%	31.18 (± 1.00)	8.11 (± 1.20)	51.64 (± 1.70)

$0.3 \pm 0.05\%$ were observed for the 6Neat filament. This explains the brittle nature of the 6Neat filament, which tends to break during 3D printing. In contrast, the plasticized 6BlankTA10 filaments exhibited the highest tensile strength of 40.08 ± 1.8 MPa. The increase in tensile strength can be attributed to the presence of structurally stable PLA crystalline

domains in the 6BlankTA10 filaments. However, the minimal increase in % elongation at break of the 6BlankTA10 filaments could be due to the loss of plasticizer during crystallization. Furthermore, the tensile strength of the bionanocomposite filaments TA10CNF1% and TA10CNF3% was 29.26 ± 1.8 MPa and 31.18 ± 1.0 MPa, respectively.

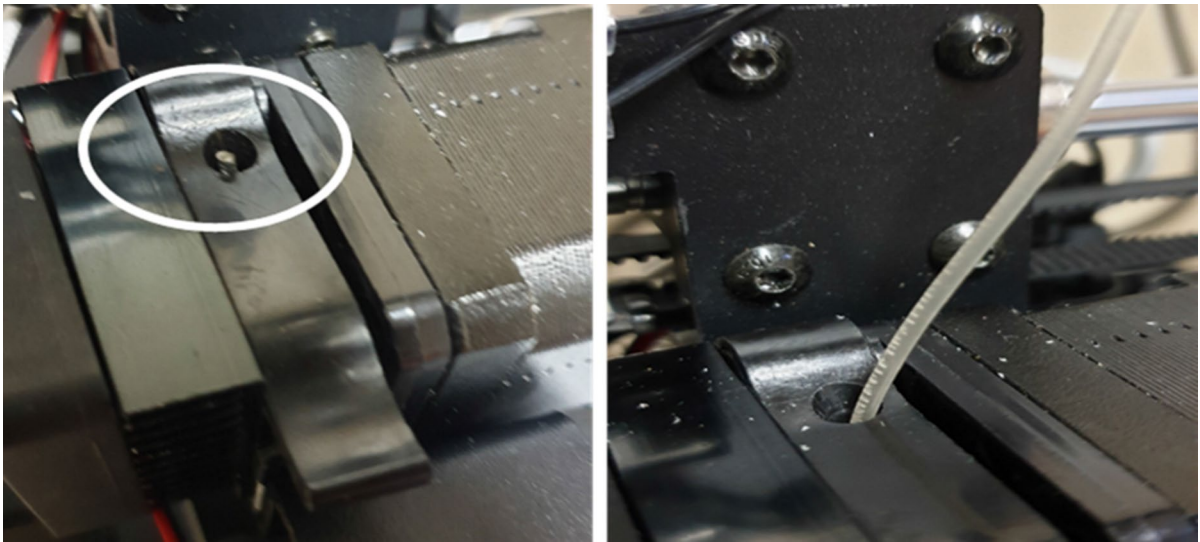


Fig. 11 The brittle behaviour of PLA before (left) and after (right) introduction of plasticizer (TA) and cellulose nanofibrils (CNFs). The circled area denotes the stem of the 6Neat filament that broke during 3D printing

The bionanocomposite filaments presented higher tensile strength compared to the virgin (6Neat) filament. This increase in tensile strength can be attributed to the reinforcing effect of CNFs. Furthermore, the superior retention of TA plasticizer is confirmed by the high elongation at break values of the bionanocomposite filaments. The %–elongation results of the bionanocomposite filaments also suggest higher amorphous composition in the PLA. Higher amorphous content and increased PLA flexibility are

known to correspond to decreased tensile strength (Paul et al. 2021). The flexibility resulting from the incorporation of both TA and CNF has effectively addressed the recurring issue of filament breakage during 3D printing, as shown in Fig. 11.

FDM 3D printer optimization

The majority of desktop FDM 3D printers, akin to the one employed in this study, are initially

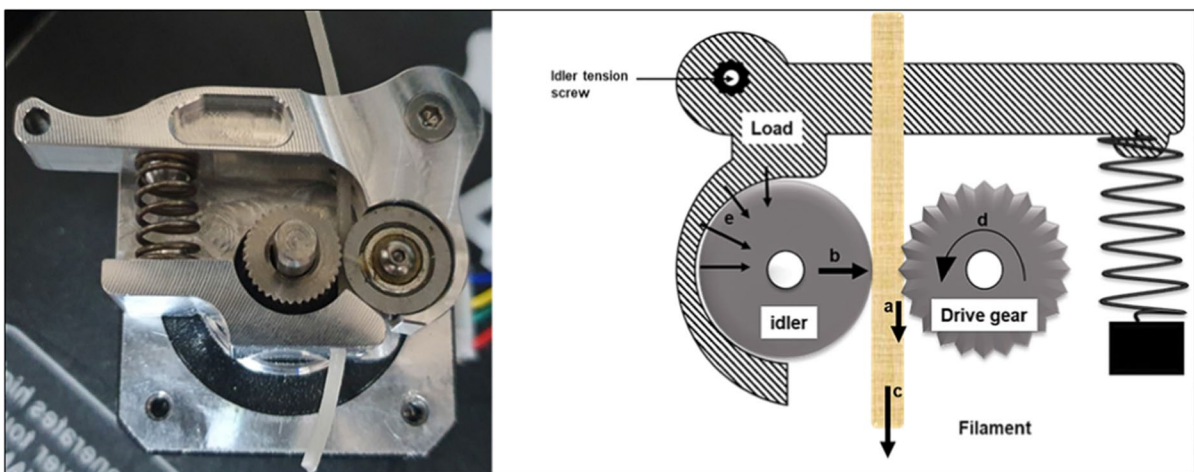


Fig. 12 The filament feeding mechanism; actual image (left), and schematic outline (right)

calibrated to accommodate thermoplastic filaments with diameters of 1.75 mm. The filaments with slightly smaller diameters generated in this research magnify the risk of under-extrusion, which stems from inadequate filament feeding. Thus, it was imperative to make several adjustments to the filament feeding mechanism of the FDM 3D printer. Adjustments were executed on the 3D printer to ensure optimal filament contact and substantial force application within the feeding mechanism. This entailed augmenting the filament tension, thereby amplifying the load on the filament. The schematic in Fig. 12 delineates the internal structure of the FDM 3D printer's feeding mechanism. The key components encompass a tension-inducing spring loading mechanism, a serrated drive gear, and a smooth idler. As the filament traverses the feeding mechanism, the idler experiences force, and the serrated drive gear imprints a slight impression onto the filament (Hermann 2022). This establishes sufficient frictional force on the filament, enabling the efficient transfer of torque generated by the rotating drive gear (denoted as "d" in Fig. 13).

The force applied by the spring load (indicated as b and e in Fig. 12) can be fine-tuned by adjusting the idler tension screw, wherein the downward force pushing the filament out is marked as a and c in Fig. 12. However, meticulous calibration of the idler tensioning screw is essential, as excessive tightening

can lead to filament grinding, crushing, or flattening. Conversely, inadequate friction on the filament can cause slipping and sliding, resulting in under-extrusion and excessive strain on the drive motor. As such, the idler screw was slightly tightened using a torque wrench during the 3D printing operation of TA10CNF1% and TA10CNF3%. For the 6BlankTA10 filaments, the tension screw was tightened further to ensure adequate friction. Subsequently, the filaments were unloaded from the feeding mechanism and subjected to visual examination for any indications of grinding. Finally, the successful 3D printing of the objects depicted in Fig. 13 was achieved through the implementation of the fine-tuning steps, combined with the processing conditions detailed in the methodology section.

Morphological analysis of 3D printed specimen

The gauge length regions within the internal structure of each 3D printed tensile specimen were examined using a scanning electron microscope (SEM), as shown in Fig. 14. The tensile specimens were cryo-fractured after soaking them in liquid nitrogen for 5 min. The SEM images at an $\times 19$ magnification level, as depicted in Fig. 14, revealed the presence of numerous empty voids within the 3D-printed tensile specimens. These voids were predominantly concentrated along the Y-axis of printing. The images also



Fig. 13 FDM 3D printed items using PLA/CNF bionanocomposite filaments

showed the absence of layer bonding between parallel deposited layers. Despite setting the extrusion width to 400 μm , measurements taken from the SEM images revealed that the final extrusion width fell below the intended specifications. (Additional information in S3). This observation could be attributed to factors such as under-extrusion of PLA, irregular filament diameter, inadequate compression, and the shrinkage of the fused deposited layers (Fig. 15).

Tensile properties 3D printed tensile specimens

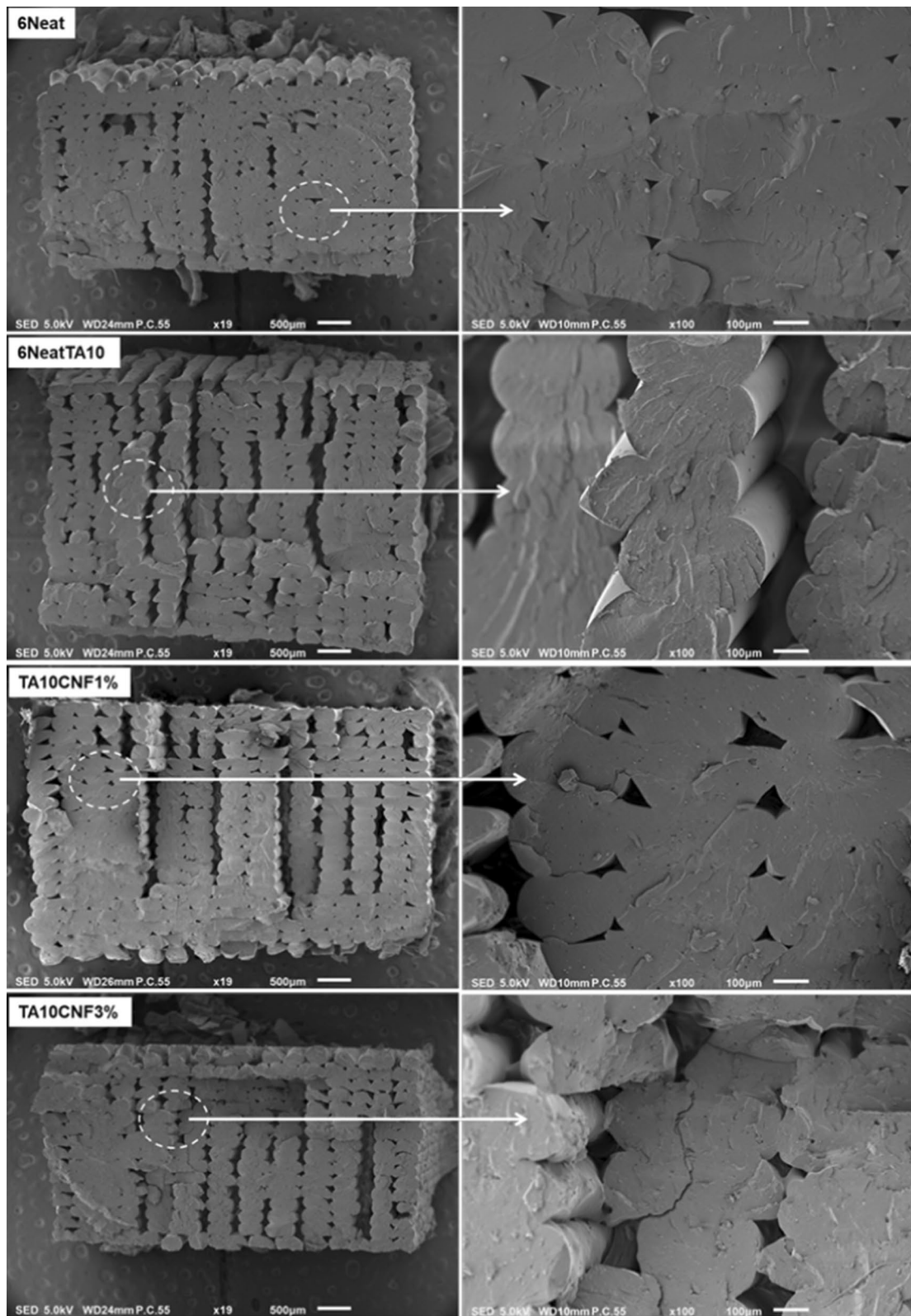
The results obtained from the tensile analysis of the 3D printed specimens are represented in Table 5. The tensile strength of the 6Neat specimen was 22.7 (± 0.07) MPa, at a maximum breaking force of 671.0 (± 0.2) N. Interestingly, these values closely resemble the tensile strength reported for compression-moulded PLA6202D by Modi et al. (2013), which was reported as 29.8 ± 6.3 MPa. The slightly lower tensile strength of the 3D-printed 6Neat specimen is probably due to high porosity, low compression, and inadequate layer adhesion. Meanwhile, the 6BlankTA10 specimens exhibited tensile strength and break force of 27.8 (± 0.12) MPa and 671.0 (± 0.2) N respectively. The elongation at break, however, was quite low for both 6Neat and 6BlankTA10. Though plasticization was expected to improve flexibility and ductility in the 6BlankTA10 specimen, this was not the case with 6BlankTA10 showing very low values of elongation at break. It is quite apparent that increased PLA crystallization and the consequent phase separation of TA resulted in low plasticizer retention in 6BlankTA10. The TA10CNF1% bionanocomposite specimen exhibited a 12% increase in the tensile strength (25.43 (± 0.28) MPa) compared to the 6Neat specimen (22.70 ± 0.07 MPa). Conversely, the tensile strength of the TA10CNF3% bionanocomposite specimen (22.41 (± 2.52) MPa) was comparable to the tensile strength of the 6Neat specimen.

Furthermore, the inclusion of TA plasticizer resulted in a slight decrease in the tensile modulus of the PLA (6Neat) from 2115.50 (± 0.71) MPa to 1962.90 (± 18.53) MPa (Table 5). However, the tensile modulus of the bionanocomposite specimens increased by 12% and 20% with the addition of 1%

CNFs (TA10CNF1%) and 3% CNFs (TA10CNF3%), respectively. The observed increase in stiffness is characteristic of PLA bionanocomposites reinforced with plant-based natural fibres (Xiao et al. 2019; Fortunati et al. 2012). However, the interfacial adhesion between the CNFs and PLA matrix is mostly due to physical interactions (Clarkson et al. 2018). However, the interfacial adhesion between the PLA matrix and natural fibres is usually enhanced by the formation of transcrystalline layers, as reported by Huan Xu et al. (2014). The authors concluded that the formation of prevailing transcrystalline layers was initiated by the nucleating effect of natural fibre and accelerated by increased polymer chain mobility induced by the plasticizer resulting in improved tensile strength (Huan Xu et al. 2014).

Table 5 also provides the average density (ρ) of all the tensile specimens, and a direct correlation is observed between density and tensile modulus (stiffness) across all the samples. The average density of the 3D printed 6Neat specimen was approximately 1.1795 g/cm³, representing a 2.25% decrease compared to the density of the original PLA6202D pellets ($\rho = 1.2067 \pm 0.08$ g/cm³). The reduction in density of the 6Neat specimen can be attributed to high porosity. This decrease in density by 7.19% in the 6BlankTA10 specimen can be attributed to the loss of plasticizer and the resulting increase in porosity. Furthermore, the bionanocomposite filaments containing 1% and 3% CNF exhibited comparable bulk density to that of the PLA6202D pellets. This is likely a result of improved plasticizer retention, enhanced compression during processing, and the presence of fewer or smaller pores. These factors contribute to a more compact and homogeneous structure, leading to a density that is closer to the original PLA material.

Furthermore, the substantial increase in elongation for the TA10CNF1% (105.17 $\pm 32.9\%$) and TA10CNF3% (78.71 ($\pm 32.9\%$) specimens can be attributed to successful plasticization, leading to improved PLA molecular chain mobility. This allowed the low molecular weight TA to penetrate the amorphous PLA domains, effectively retarding crystallization. Additionally, the CNFs are believed to absorb excess TA that is exuded from the crystalline domains. The stress vs. strain curves for all



◀**Fig. 14** SEM images of cryofracture surfaces of Top; 6Neat, 6NeatTA10, TA10CNF1% and TA10CNF3%. Bottom×100 magnification of encircled areas

the samples is depicted in Fig. 16. The stress–strain behaviour of the 6Neat and 6BlankTA10 specimens displayed brittle failure patterns, with a slight strain hardening observed in 6BlankTA10. This strain hardening contributed to the increased tensile strength of 6BlankTA10. Conversely, the stress–strain behaviour of the bionanocomposite specimens in Fig. 16 exhibited ductile failure characteristics. These specimens showed a distinct sequence of events: a sharp stress increase, a yielding point, strain softening, ductile stretching, and eventual rupture. Lastly, a significant decrease in the breaking force was observed between 6Neat, 6BlankTA10 and TA10CNF1% specimens. However, a slightly lower force was required to fracture the TA10CNF3% specimen.

Figure 16 illustrates images of the 3D-printed tensile specimens before and after undergoing uniaxial tensile testing. The TA10CNF1% and TA10CNF3% bionanocomposite specimens exhibited similar ductile fracture behaviour. The ductile stretching of these specimens led to a whitening effect in the area around the gauge length region. This whitening effect is a result of crazing (micro-void formation) and strain-induced crystallization, wherein the initially random PLA polymer chains become mechanically oriented into more ordered domains (Drumright et al. 2000). The occurrence of strain-induced crystallization produces a strain-hardening effect, which is responsible for the stable tensile stress during ductile stretching as shown in Fig. 15. Conversely, the tensile fracture of 6Neat and 6NeatTA10 specimens occurred between the grip section and gauge length. The fact that the tensile fracture occurred at the joint between the grip section and the gauge length suggests the presence of mechanically weak areas in the 3D-printed tensile specimen. These weak points likely contributed to the failure of the specimen at that location.

Summary

In this work, PLA/CNF bionanocomposite filaments were developed and successfully printed on an FDM 3D printer to form several prototypes. The cellulose nanofibrils (CNFs) used were successfully isolated

from sawdust via chemo-mechanical methods. Morphological and crystallinity analysis revealed that the CNFs are composed of dense networks of cellulose fibrils with an average degree crystalline of 79.3%. The subsequent thermal analysis confirmed that the extracted CNFs were thermally stable within the intended processing temperature. A solvent casting masterbatch step was adopted to achieve good dispersion of CNFs in the PLA matrix. This step was proceeded by a low-temperature melt mixing and filament extrusion step. This low-temperature profile was enabled by the incorporation of a bio-based plasticizer (triacetin) which improved processibility. In addition, the plasticizing effect of TA facilitated low printing temperatures and eliminated the brittle fracturing of filaments during the FDM 3D printing process. Furthermore, better consistencies in filament diameter were achieved for the PLA/CNF bionanocomposites. Nevertheless, a series of adjustments were performed on the filament feeding mechanism of the FDM 3D printer to optimize the printing process. Furthermore, the aggregation of CNFs observed in Fig. 10 did not result in the blockage of the FDM printer nozzle during the 3D printing process.

Furthermore, the FTIR chemical analysis revealed a transmittance peak around 925 cm^{-1} in PLA/CNF bionanocomposite spectra, indicative of increased crystallinity. Results from thermogravimetric analysis (TGA) of the bionanocomposites revealed a decrease in thermal stability. This was attributed to the early onset of thermal hydrolysis induced by water emanating from the CNF. However, the filaments were still useable since the thermal decomposition occurred well above the temperature used during 3D printing. A noticeable increase in the flexibility of PLA/CNF composites was attained due to the plasticizing effects of TA. This improvement was reflected in the high elongation at break values of PLA/CNF_{1%}/TA₁₀ (105.17%) and PLA/CNF_{3%}/TA₁₀ (78.71%). However, the increase in % elongation resulted in a slight reduction in ultimate tensile strength. The images of the tensile specimens of PLA/CNF_{1%}/TA₁₀ and PLA/CNF_{3%}/TA₁₀ bionanocomposites both showed ductile fracture behaviour, whereas the 6neat and 6NeatTA10 control sample exhibited brittle fracture behaviour. Future work would focus on investigating the crystallization behaviour of PLA/CNF bionanocomposites, adoption of higher molecular

Fig. 15 Stress vs Strain behaviour of 3D printed specimens of TA10CNF1% (green), TA10CNF3% (red); insert 6Neat (black) and 6NeatTA10 (blue)

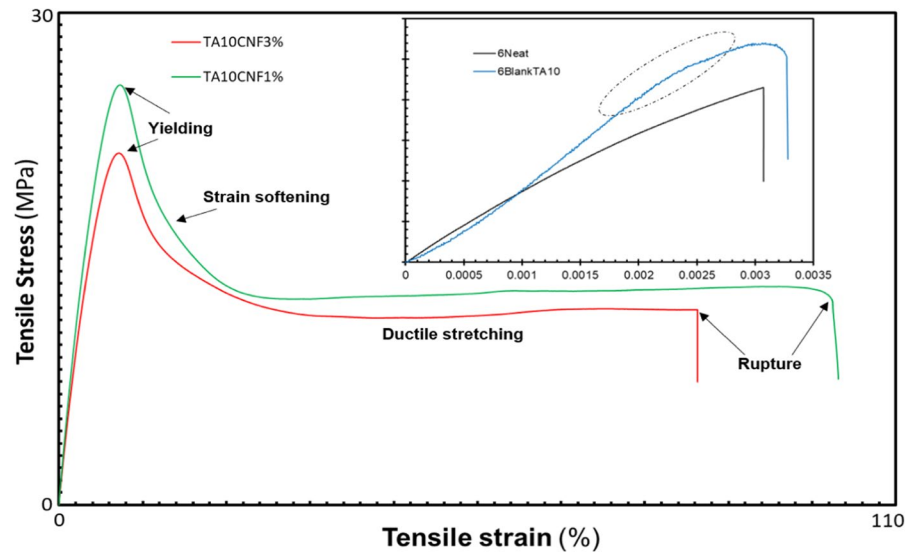


Table 5 Results from the tensile analysis and density of 3D printed dumbbell specimens

Sample description	Tensile strength (MPa)	Elongation at Break (%)	Maximum breaking force (N)	Tensile Modulus (MPa)	Density (g/cm ³)
6Neat	22.70 (±0.07)	0.11 (±0.02)	556.50 (±0.70)	2115.50 (±0.71)	1.1795 (±0.02)
6BlankTA10	27.80 (±0.12)	0.14 (±0.04)	671.00 (±0.20)	1962.90 (±18.53)	1.1199 (±0.12)
TA10CNF1%	25.43 (±0.28)	105.17 (±32.90)	623.00 (±4.20)	2378.75 (±55.51)	1.2018 (±0.02)
TA10CNF3%	22.41 (±2.52)	78.71 (±32.90)	549.00 (±65.50)	2542.33 (±108.87)	1.2256 (±0.03)



Fig. 16 Tensile test specimen of 6Neat, 6NeatTA10, TA10CNF1% and TA10CNF3% before (left) and after (right) uniaxial tensile analysis

weight plasticizers and improving the PLA/CNF compatibility.

Acknowledgments Funding from the Department of Science and Innovation (DSI), South Africa—Biorefinery Consortium Project—under the DSI Bioeconomy program is gratefully

acknowledged by the authors. The Centre for Rubber Science and Technology (CRST), Nelson Mandela University, South Africa is duly acknowledged for instrumentation and testing equipment.

Authors contribution Conceptualization, VCA and MJJ; methodology, VCA and TCM; 3D printing, VCA; formal analysis, VCA and SPH; investigation, VCA, TCM and EEF; resources, MJJ, SPH and EEF; data curation, VCA and EEF; writing—original draft preparation, VCA, MJJ, and SPH; writing—review and editing, VCA, MJJ, and SPH; visualization, VCA; supervision, MJJ, and SPH; project administration, MJJ, and SPH; funding acquisition, MJJ. All authors have read and agreed to the published version of the manuscript.

Funding Open access funding provided by Mintek. This research was funded by the Department of Science and Innovation (DSI), South Africa—Biorefinery Consortium Project—Under the DSI Bioeconomy program, Grant number DST/CON0188/2017.

Data availability The data generated/analysed, and materials prepared under the current study are available from the corresponding author on reasonable request.

Declarations

Conflict of interest The authors declare that they have no known competing financial interests or any personal connections that could have appeared to influence the work reported.

Ethical approval This research article does not contain studies involving human participants or animals performed by any of the authors.

Consent for publication All authors have approved the final version of the manuscript.

Open Access This article is licensed under a Creative Commons Attribution 4.0 International License, which permits use, sharing, adaptation, distribution and reproduction in any medium or format, as long as you give appropriate credit to the original author(s) and the source, provide a link to the Creative Commons licence, and indicate if changes were made. The images or other third party material in this article are included in the article's Creative Commons licence, unless indicated otherwise in a credit line to the material. If material is not included in the article's Creative Commons licence and your intended use is not permitted by statutory regulation or exceeds the permitted use, you will need to obtain permission directly from the copyright holder. To view a copy of this licence, visit <http://creativecommons.org/licenses/by/4.0/>.

References

- Agarwal UP, Ralph SA, Baez C, Reiner RS (2021) Contributions of crystalline and non-crystalline cellulose can occur in the same spectral regions: evidence based on Raman and IR and its implication for crystallinity measurements. *Biomacromol* 22:1357–1373. <https://doi.org/10.1021/acs.biomac.0c01389>
- Armentano I, Bitinis N, Fortunati E, Mattioli S, Rescignano N, Verdejo R, López-Manchado MA, Kenny JM (2013) Multifunctional nanostructured PLA materials for packaging and tissue engineering. *Prog Polym Sci* 38(10–11):1720–1747. <https://doi.org/10.1016/j.progpolymsci.2013.05.010>
- Beltrán FR, de la Orden MU, Lorenzo V, Pérez E, Cerrada ML, Urreaga M (2016) Water-induced structural changes in poly (lactic acid) and PLLA-clay nanocomposites. *Polymer* 107:211–222. <https://doi.org/10.1016/j.polymer.2016.11.031>
- Chakraborty A, Sain M, Kortschot M (2006) Reinforcing potential of wood pulp-derived microfibers in a PVA matrix. *Holzforschung* 60(1):53–58. <https://doi.org/10.1515/HF.2006.010>
- Clarkson CM, El Awad Azrak SM, Chowdhury R, Shuvo SN, Snyder J, Schueneman G et al (2018) Melt spinning of cellulose nanofibril/poly(lactic acid) (CNF/PLA) composite fibres for high stiffness. *ACS Applied Polymer Materials* 1(2):160–168. <https://doi.org/10.1021/acsapm.8b00030>
- Clarkson CM, Azrak SM, Schueneman GT, Snyder JF, Youngblood JP (2020) Crystallization kinetics and morphology of small concentrations of cellulose nanofibrils (CNFs) and cellulose nanocrystals (CNCs) melt-compounded into poly (lactic acid) (PLA) with a plasticizer. *Polymer* 187:122101. <https://doi.org/10.1016/j.polymer.2019.122101>
- Dong J, Li M, Zhou L, Lee S, Mei C, Xu X, Wu Q (2017) The influence of grafted cellulose nanofibrils and post extrusion annealing treatment on selected properties of poly (lactic acid) filaments for 3D printing. *J Polym Sci, Part B: Polym Phys* 55(11):847–855. <https://doi.org/10.1002/polb.24333>
- Drumright RE, Gruber PR, Henton DE (2000) Poly(lactic acid) technology. *Adv Mater* 12(23):1841–1846. [https://doi.org/10.1002/1521-4095\(200012\)12:23%3C1841::AID-ADMA1841%3E3.0.CO;2-E](https://doi.org/10.1002/1521-4095(200012)12:23%3C1841::AID-ADMA1841%3E3.0.CO;2-E)
- Ferreira RTL, Amatte IC, Dutra TA, Bürger D (2017) Experimental characterization and micrography of 3D printed PLA and PLA reinforced with short carbon fibres. *Compos B Eng* 124:88–100. <https://doi.org/10.1016/j.composb.2017.05.013>
- Fortunati E, Armentano I, Zhou Q, Iannoni A, Saino E, Visai L, Berglund LA, Kenny JM (2012) Multifunctional bio-nanocomposite films of poly (lactic acid), cellulose nanocrystals and silver nanoparticles. *Carbohydr Polym* 87(2):1596–1605. <https://doi.org/10.1016/j.carbpol.2011.09.066>
- Gohar S, Hussain G, Ali A, Ahmad H (2021) Mechanical performance of honeycomb sandwich structures built by FDM printing technique. *J Thermoplast Compos Mater* 36(1):182–200. <https://doi.org/10.1177/0892705721997892>
- Harte I, Birkinshaw C, Jones E, Kennedy J, DeBarra E (2013) The effect of citrate ester plasticizers on the thermal and mechanical properties of poly (DL-lactide). *J Appl Polym Sci* 127(3):1997–2003. <https://doi.org/10.1002/app.37600>

- Hermann S (2022) 'How to set extruder tension?'. Online Blogpost: CNC KITCHEN. <https://www.cnckitchen.com/blog/how-to-set-extruder-tension> Accessed 10 June 2022.
- Herrera N, Mathew AP, Oksman K (2015) Plasticized polylactic acid/cellulose nanocomposites prepared using melt-extrusion and liquid feeding: mechanical, thermal and optical properties. *Compos Sci Technol* 106:149–155. <https://doi.org/10.1016/j.compscitech.2014.11.012>
- Iwatake A, Nogi M, Yano H (2008) Cellulose nanofibre-reinforced polylactic acid. *Compos Sci Technol* 68(9):2103–2106. <https://doi.org/10.1016/j.compscitech.2008.03.006>
- Jiang X, Luo Y, Tian X, Huang D, Reddy N, Yang Y (2010) Chemical Structure of Poly(Lactic Acid). In: Grossman RF, Nwabunma D, Auras R, Lim LT, Selke SEM, Tsuji H (eds) *Poly(Lactic Acid) Synthesis, Structures, Properties, Processing, and Applications*. Wiley, pp 67–82. <https://doi.org/10.1002/9780470649848.ch6>
- John MJ, Dyanti N, Mokhena T, Agbakoba V, Sithole B (2021) Design and development of cellulosic bionanocomposites from forestry waste residues for 3D printing applications. *Materials* 14(13):3462. <https://doi.org/10.3390/ma14133462>
- Jonoobi M, Harun J, Mathew AP, Oksman K (2010) Mechanical properties of cellulose nanofibre (CNF) reinforced polylactic acid (PLA) prepared by twin screw extrusion. *Composite Science and Technology* 70(12):1742–1747. <https://doi.org/10.1016/j.compscitech.2010.07.005>
- Kister G, Cassanas G, Vert M (1998) Effects of morphology, conformation and configuration on the IR and Raman spectra of various poly(lactic acid). *Polymer* 39(2):267–273. [https://doi.org/10.1016/S0032-3861\(97\)00229-2](https://doi.org/10.1016/S0032-3861(97)00229-2)
- Kouadri I, Satha H (2018) Extraction and characterization of cellulose and cellulose nanofibrils from *Citrullus colocynthis* seeds. *Ind Crops Prod* 124:787–796. <https://doi.org/10.1016/j.indcrop.2018.08.051>
- Lacerda CV, Carvalho MJ, Rattou AR, Soares IP, Borges LE (2015) Synthesis of triacetin and evaluation on motor. *J Braz Chem Soc* 26:1625–1631. <https://doi.org/10.5935/0103-5053.20150133>
- Li L, Chen Y, Yu T, Wang N, Wang C, Wang H (2019) Preparation of polylactic acid/TEMPO-oxidized bacterial cellulose nanocomposites for 3D printing via Pickering emulsion approach. *Compos Commun* 16:162–167. <https://doi.org/10.1016/j.coco.2019.10.004>
- Ljungberg N, Wesslen B (2002) The effects of plasticizers on the dynamic mechanical and thermal properties of poly(lactic acid). *J Appl Polym Sci* 86(5):1227–1234. <https://doi.org/10.1002/app.11077>
- Martin O, Avérous L (2001) Poly(lactic acid): plasticization and properties of biodegradable multiphase systems. *Polymer* 42(14):6209–6219. [https://doi.org/10.1016/S0032-3861\(01\)00086-6](https://doi.org/10.1016/S0032-3861(01)00086-6)
- Mochane MJ, Mokhena TC, Sadiku ER, Ray SS, Mofokeng TG (2019) Green polymer composites based on polylactic acid (PLA) and fibers. In: Gnanasekaran D (ed) *Green Biopolymers and their Nanocomposites*. Materials Horizons: From Nature to Nanomaterials. Springer, Singapore. https://doi.org/10.1007/978-981-13-8063-1_2
- Modi S, Koelling K, Vodovotz Y (2013) Assessing the mechanical, phase inversion, and rheological properties of poly-[(R)-3-hydroxybutyrate-co-(R)-3-hydroxyvalerate] (PHBV) blended with poly-(l-lactic acid)(PLA). *Eur Polymer J* 49(11):3681–3690. <https://doi.org/10.1016/j.eurpolymj.2013.07.036>
- Mohammed MI, Mohan M, Das A, Johnson MD, Badwal PS, McLean D, Gibson I (2017) A low carbon footprint approach to the reconstitution of plastics into 3D-printer filament for enhanced waste reduction. In: *DesTech 2016: Proceedings of the International Conference on Design and Technology*. Knowledge Engineering, 234–241. <https://doi.org/10.18502/keg.v2i2.621>
- Mokhena TC, Sefadi JS, Sadiku ER, John MJ, Mochane MJ, Mtibe A (2018) Thermoplastic processing of PLA/cellulose nanomaterials composites. *Polymer*. <https://doi.org/10.3390/polym10121363>
- Mokhena TC, Mochane MJ, Sadiku ER, Agboola O, John MJ (2019) Opportunities for PLA and Its Blends in Various Applications. In: Gnanasekaran D (ed) *Green Biopolymers and their Nanocomposites*. From Nature to Nanomaterials. Springer, Singapore, Materials Horizons. https://doi.org/10.1007/978-981-13-8063-1_3
- Mokhena TC, Sadiku ER, Mochane MJ, Ray SS (2021) Mechanical properties of fire retardant wood-plastic composites: a review. *Express Polym Lett* 15:744–780. <https://doi.org/10.3144/expresspolymlett.2021.61>
- Moon RJ, Martini A, Nairn J, Simonsen J, Youngblood J (2011) Cellulose nanomaterials review: structure, properties and nanocomposites. *Chem Soc Rev* 40(7):3941–3994. <https://doi.org/10.1039/C0CS00108B>
- Motaung TE, Mtibe A (2015) Alkali treatment and cellulose nanowhiskers extracted from maize stalk residues. *Mater Sci Appl* 6(11):1022. <https://doi.org/10.4236/msa.2015.611102>
- Mtibe A, Langaniso LZ, Mathew AP, Oksman K, John MJ, Anandjiwala RD (2015) A comparative study on properties of micro and nano papers produced from cellulose and cellulose nanofibers. *Carbohydr Polym* 118:1–8. <https://doi.org/10.1016/j.carbpol.2014.10.007>
- Müller M, Burghammer M, Sugiyama J (2006) Direct investigation of the structural properties of tension wood cellulose microfibrils using microbeam X-ray fibre diffraction. *Holzforschung*. <https://doi.org/10.1515/HF.2006.078>
- Murphy CA, Collins MN (2018) Microcrystalline cellulose reinforced polylactic acid bionanocomposite filaments for 3D printing. *Polym Compos* 39(4):1311–1320. <https://doi.org/10.1002/pc.24069>
- Nishiyama Y, Langan P, Chanzy H (2002) Crystal structure and hydrogen-bonding system in cellulose I β from synchrotron X-ray and neutron fibre diffraction. *J Am Chem Soc* 124(31):9074–9082. <https://doi.org/10.1021/ja0257319>
- Özdilli Ö (2021) Comparison of the surface quality of the products manufactured by the plastic injection molding and SLA and FDM Methods. *Int J Eng Res Dev* 13(2):428–437. <https://doi.org/10.29137/umagd.762942>
- Pan AQ, Huang ZF, Guo RJ, Liu J (2016) Effect of FDM process on the adhesive strength of polylactic acid (PLA) filament. *Key Eng Mater* 667:181–186. <https://doi.org/10.4028/www.scientific.net/KEM.667.181>
- Paul UC, Fragouli D, Bayer IS, Zych A, Athanassiou A (2021) Effect of green plasticizer on the performance of microcrystalline cellulose/polylactic acid

- bionanocomposites. *ACS Appl Polym Mater* 3(6):3071–3081. <https://doi.org/10.1021/acsapm.1c00281>
- Rasheed M, Jawaid M, Karim Z, Abdullah LC (2020) Morphological, physiochemical and thermal properties of microcrystalline cellulose (MCC) extracted from bamboo fibre. *Molecules* 25(12):2824. <https://doi.org/10.3390/molecules25122824>
- Sato S, Gondo D, Wada T, Kanehashi S, Nagai K (2013) Effects of various liquid organic solvents on solvent-induced crystallization of amorphous poly (lactic acid) film. *J Appl Polym Sci* 129(3):1607–1617. <https://doi.org/10.1002/app.38833>
- Södergård A, Stolt M (2002) Properties of lactic acid based polymers and their correlation with composition. *Prog Polym Sci* 27(6):1123–1163. [https://doi.org/10.1016/S0079-6700\(02\)00012-6](https://doi.org/10.1016/S0079-6700(02)00012-6)
- Tekinalp HL, Meng X, Lu Y, Kunc V, Love LJ, Peter WH, Ozcan S (2019) High modulus bionanocomposites via additive manufacturing: Cellulose nanofibril networks as “microsponges.” *Compos B Eng* 173:106817. <https://doi.org/10.1016/j.compositesb.2019.05.028>
- Terinte N, Ibbett R, Schuster KC (2011) Overview on native cellulose and microcrystalline cellulose I structure studied by X-ray diffraction (WAXD): comparison between measurement techniques. *Lenzinger Berichte* 89(1):118–131
- Tonoli GHD, Holtman KM, Glenn G, Fonseca A, Wood D, Williams T, Sa VA, Torres L, Klameczynski A, Orts WJ (2016) Properties of cellulose micro/nanofibrils obtained from eucalyptus pulp fibre treated with anaerobic digestate and high shear mixing. *Cellulose* 23(2):1239–1256. <https://doi.org/10.1007/s10570-016-0890-5>
- Vaitkus A, Merkys A, Gražulis S (2021) Validation of the crystallography open database using the crystallographic information framework. *J Appl Crystallogr* 54(2):661–672. <https://doi.org/10.1107/S1600576720016532>
- Wang B, Sain M (2007) Dispersion of soybean stock-based nanofibre in a plastic matrix. *Polym Int* 56(4):538–546. <https://doi.org/10.1002/pi.2167>
- Wang Z, Xu J, Lu Y, Hu L, Fan Y, Ma J, Zhou X (2017) Preparation of 3D printable micro/nano cellulose-poly(lactic acid) (MNC/PLA) composite wire rods with high MNC constitution. *Ind Crops Prod* 109:889–896. <https://doi.org/10.1016/j.indcrop.2017.09.061>
- Wang A, Zhou W, Huang A, Chen M, Chen J, Tian Q, Xu J (2020a) Modifying the Zn anode with carbon black coating and nanofibrillated cellulose binder: a strategy to realize dendrite-free Zn-MnO₂ batteries. *J Colloid Interface Sci* 577:256–264. <https://doi.org/10.1016/j.jcis.2020.05.102>
- Wang Q, Ji C, Sun L, Sun J, Liu J (2020b) Cellulose nanofibrils filled poly (lactic acid) bionanocomposite filament for FDM 3D printing. *Molecules* 25(10):2319. <https://doi.org/10.3390/molecules25102319>
- West UG, Ashby MF (2004) The mechanical efficiency of natural materials. *Phil Mag* 84(21):2167–2186. <https://doi.org/10.1080/14786430410001680935>
- Xiao X, Chevali VS, Song P, He D, Wang H (2019) Poly(lactide)/hemp hurd bionanocomposites as sustainable 3D printing feedstock. *Compos Sci Technol* 184:107887. <https://doi.org/10.1016/j.compscitech.2019.107887>
- Xie F, Bao J, Zhuo L, Zhao Y, Dang W, Si L, Yao C, Zhang M, Lu Z (2020) Toward high-performance nanofibrillated cellulose/aramid fibril paper-based composites via polyethyleneimine-assisted decoration of silica nanoparticle onto aramid fibril. *Carbohydr Polym* 245:116610. <https://doi.org/10.1016/j.carbpol.2020.116610>
- Xu H, Xie L, Jiang X, Li XJ, Li Y, Zhang ZJ, Zhong GJ, Li ZM (2014) Toward stronger transcrySTALLINE layers in poly (l-lactic acid)/natural fibre bionanocomposites with the aid of an accelerator of chain mobility. *J Phys Chem B* 118(3):812–823. <https://doi.org/10.1021/jp409021q>
- Xu W, Pranovich A, Uppstu P, Wang X, Kronlund D, Hemming J et al (2018) Novel biorenewable composite of wood polysaccharide and polylactic acid for three-dimensional printing. *Carbohydr Polym* 187:51–58. <https://doi.org/10.1016/j.carbpol.2018.01.069>
- Yousefi H, Faezipour M, Hedjazi S, Mousavi MM, Azusa Y, Heidari AH (2013) Comparative study of paper and nano paper properties prepared from bacterial cellulose nanofibrils and fibres/ground cellulose nanofibrils of canola straw. *Ind Crops Prod* 43:732–737. <https://doi.org/10.1016/j.indcrop.2012.08.030>
- Zou R, Xia Y, Liu S, Hu P, Hou W, Hu Q, Shan C (2016) Isotropic and anisotropic elasticity and yielding of 3D printed material. *Compos B Eng* 99:506–513. <https://doi.org/10.1016/j.compositesb.2016.06.009>

Publisher's Note Springer Nature remains neutral with regard to jurisdictional claims in published maps and institutional affiliations.